PAPER • **OPEN ACCESS**

Graphene direct growth by microwave PECVD on h-BN films deposited by reactive HIPIMS

To cite this article: Šarūnas Meškinis *et al* 2025 *Nano Ex.* **6** 025007

NANO EXPRESS

PAPER

Graphene direct growth by microwave PECVD on h-BN films deposited by reactive HIPIMS

Šarūnas Meškinis, Šarūnas Jankauskas, Andrius Vasiliauskas, Vytautas Stankus, Asta Guobienė, Kipras Lukoševičius, Augmantas Jasutis and Rimantas Gudaitis

Institute of Materials Science, Kaunas University of Technology, K Baršausko 59, LT-51423, Kaunas, Lithuania

E-mail: sarunas.meskinis@ktu.lt **and** sarunas.jankauskas@ktu.lt

Keywords: graphene, h-BN, HIPIMS, AFM, CAFM, photoelectric properties, direct synthesis by microwave PECVD

Supplementary material for this article is available online

OPEN ACCESS

RECEIVED
10 February 2025

REVISED
30 April 2025

ACCEPTED FOR PUBLICATION
9 May 2025

PUBLISHED
20 May 2025

Abstract

This research explores the synthesis of graphene using microwave plasma-enhanced chemical vapor deposition (PECVD) on a hexagonal boron nitride interlayer deposited by reactive high-power impulse magnetron sputtering. The effects of h-BN interlayer composition and thickness on the graphene structure, morphology, and electronic properties were investigated using Raman scattering spectroscopy, atomic force microscopy, and conductive atomic force microscopy. The electrical and photoelectrical characteristics of the graphene/Si(100) and graphene/h-BN/Si(100) diodes were studied. It was revealed that graphene self-doping effects, primarily originating from substrate-induced charge transfer, can be partially controlled, and that the dominant defect type of graphene can be changed by varying the boron interlayer thickness. The graphene layers synthesized on the SiO_2 film were substantially smoother than those grown on the boron nitride films. Graphene grown on h-BN had a substantially greater surface current than graphene synthesized on the SiO_2 layer. There was no relationship between graphene self-doping and graphene surface conductivity. Nevertheless, it should be noted that reduced graphene self-doping was achieved even though the surface roughness of the h-BN film was significantly greater than that of the SiO_2 film or Si(100), and B–H and C–H bonds were present in some h-BN films. Tunneling is the primary reverse current charge transfer mechanism, similar to graphene/Si(100) diodes, and h-BN interlayers cannot decrease the reverse dark current. Despite these circumstances, the insertion of the h-BN interlayer resulted in a significant increase in the photocurrent, short-circuit current, and open-circuit voltage compared to those of the graphene/Si(100) heterojunction. The observed effects of the h-BN interlayer on the graphene/Si(100) diode properties were explained by the competition between the effects of the different h-BN film compositions, thicknesses, and roughness on the one hand and the influence of the graphene structure and electronic properties.

1. Introduction

The - two-dimensional hexagonal carbon nanomaterial, graphene, has captured the attention of the scientific world owing to its unmatched mechanical, optical, and electronic properties [1–3]. In particular, their use as substitute for metal electrodes and transparent conductor layers in optoelectronic devices is promising. Most notably, replacing materials containing rare chemical elements, such as indium in indium tin oxide (ITO) [4], is crucial for maintaining a cost-effective approach in device fabrication while additionally increasing device performance [5–11]. For example, by acting as an effective charge extractor in perovskite solar cells, graphene increases the power conversion efficiency to 6.7% when produced in monolayer form, and to 11.5% when a multilayer film is used [12].

To ensure that such device fabrication retains scalability and performance, direct graphene fabrication appears to be a feasible route, compared to the readily available exfoliation and transfer of graphene grown by chemical vapor deposition on catalytic copper foil [13, 14]. Graphene can be synthesized directly on different semiconductors and dielectric substrates using various vapor phase-based deposition methods. 'Conventional' chemical vapor deposition can be applied for this purpose. The graphene synthesis temperature can be significantly reduced from 1000 °C–1400 °C [15–18] to 500 °C–700 °C using high-density plasma assistance [19–21]. However, directly synthesized graphene is usually nanocrystalline and contains many grain-boundary defects [22, 23]. This limits the performance of directly synthesized graphene-based semiconductor devices and sensors [21].

The densities of grain boundaries and other defects can be significantly reduced by selecting a suitable substrate for direct graphene synthesis. In particular, graphene and hexagonal boron nitride (h-BN) share very similar hexagonal crystal lattice parameters, enabling epitaxial growth of low-defect-density graphene on boron nitride [24–29]. However, exfoliated h-BN flakes or h-BN synthesized by chemical vapor deposition (CVD) on copper foil have been used in graphene epitaxial growth experiments.

There are very few studies on graphene synthesis using h-BN interlayers grown directly onto non-catalytic substrates such as silicon or SiO_2, and existing studies ([30]) have not succeeded in synthesizing graphene with low defect density nor investigated its functional device properties. Moreover, previous studies focused solely on structural and compositional analysis of graphene without exploring optoelectronic performance. In this study, we employed high-power impulse magnetron sputtering (HIPIMS) to grow h-BN interlayers directly onto silicon at a significantly reduced temperature (800 °C) compared to the 1000 °C typically required for chemical vapor deposition (CVD) [30]. Our approach also utilizes nitrogen gas instead of hazardous ammonia borane precursors, thus enhancing safety and purity and reducing contamination risks. Additionally, by applying plasma-enhanced CVD for subsequent graphene synthesis, we lowered the required graphene growth temperature to 700 °C, substantially below the 1000 °C used in [30]. This significant reduction in synthesis temperatures offers substantial practical advantages for device integration, scalability, substrate preservation, and industrial feasibility.

Crucially, this study provides the first systematic investigation of the effects of h-BN interlayer composition and thickness on structure, morphology, electrical, photovoltaic, and photoelectric properties specifically for graphene directly synthesized on h-BN interlayers grown onto non-catalytic substrates without transfer processes. We demonstrate that graphene self-doping effects can be partially controlled and that the insertion of an optimized h-BN interlayer significantly increases the photocurrent, short-circuit current, and open-circuit voltage of graphene/Si(100) photodiodes. Additionally, our results indicate that the dominant defect type in graphene directly grown on non-catalytic substrates can be influenced by adjusting the thickness of the underlying h-BN interlayer, offering a valuable approach for tailoring graphene properties in device applications.

2. Materials and methods

In this study, monocrystalline, double-side-polished, n-type Si(100) wafers were used as substrates. The silicon wafer resistivity was in the range 1–10 Ω·cm. Some graphene samples studied by contact-mode conductive atomic force microscopy were synthesized on the 300 nm thickness SiO_2 films grown by the thermal oxidation of Si(100) to avoid the possible influence of the semiconducting Si(100) substrate. The substrates were coated by hexagonal boron nitride (h-BN) interlayers. h-BN films were deposited by high-power impulse magnetron sputtering (HIPIMS) at 800 °C. The impulse parameters were as follows: $t_{on} = 17$ μs, $t_{of} = 150$ μs, impulse current of 1.2 A, average current constant during all processes and was about ~0.12 A, average voltage of ~930 V, and distance between the substrate and magnetron cathode of 15 cm. Other interlayer deposition conditions are listed in table 1. h-BN interlayer deposition conditions were selected based on our previous study [31].

Graphene was synthesized using a microwave plasma-enhanced chemical vapor deposition system (Cyrannus Innovative Plasma Systems (Iplas) GmbH, Germany). A special enclosure was used to prevent the excessive action of direct plasma on the substrate and growing graphene layer [20, 32, 33]. Before the growth of graphene, hydrogen plasma was ignited to clean the substrate surface. The plasma power was set at 1 kW, process temperature was 700 °C, hydrogen flow was 200 sccm, pressure was 10 mbar, and cleaning time was 10 min. Subsequently, methane gas was introduced and graphene synthesis was initiated. The graphene growth process conditions were as follows: plasma power 0.7 kW, hydrogen gas flow, 75 sccm; methane gas flow, 25 sccm; pressure, 10 mBar; substrate temperature, 700 °C; synthesis time, 60 min.

Graphene/Si (100) diodes were fabricated to investigate their electrical and photoelectric properties. First, a sample consisting of graphene grown on a Si(100) piece was cleaned. Cleaning consisted of boiling in dimethylformamide and acetone, etching in a 1:1:5 solution of $NH_4OH + H_2O_2 + H_2O$, impurity removal using

Table 1. H-BN interlayer deposition conditions.

Sample no.	Substrate	N_2 flow (sccm)	h-BN film Growth time (s)	h-BN film thickness (nm)
1	Si(100)	Reference sample (no h-BN interlayer)	—	—
2	SiO_2	Reference sample (no h-BN interlayer)	—	—
3	Si(100)	152	36	1
4	Si(100)	152	108	3
5	Si(100)	152	180	5
6	Si(100)	152	360	10
7	Si(100)	152	540	15
8	Si(100)	152	720	20
9	Si(100)	152	3600	100
10	Si(100)	152	10800	300
11	Si(100)	197	33	1
12	Si(100)	197	99	3
13	Si(100)	197	165	5
14	Si(100)	197	330	10
15	Si(100)	197	495	15
16	Si(100)	197	660	20
17	Si(100)	197	3600	110
18	Si(100)	197	10800	330

a 1:50 solution of $HF + H_2O$, and etching using a 1:1:6 solution of $HCl + H_2O_2 + H_2O$. The Al back contact was e-beam-evaporated on the uncoated side of the silicon. Cr/Cu electrodes were deposited on graphene through a mask with 500 μm circular holes. The thicknesses of the Cr interlayer and Cu layer were 20 nm and 200 nm, respectively. More information on the fabrication of graphene/Si(100) diodes can be found elsewhere [32, 33].

The boron nitride film thickness was determined using a laser ellipsometer Gaertner L-115 operating with a He–Ne laser ($\lambda = 632.8$ nm). The thickness of films thinner than 20 nm was evaluated by considering the deposition rate estimated for thicker films and the deposition time.

Raman scattering measurements were performed using a Raman scattering spectrometer InVia (Renishaw, Wotton-, UK). The excitation beam from a diode laser with a wavelength of 532 nm was focused on the sample using a 50× objective lens (NA = 0.75; Leica, Solms, Germany). The Raman spectra were measured at least three times at different sample locations and the average values were calculated. The D, G, D′, and 2D peaks were fitted using Lorentzian functions. The intensity ratio of the 2D and G peaks (I(2D)/I(G)) was used to estimate the number of graphene layers [34]. The I(2D)/I(G) ratio decreased with increasing number of graphene layers. The intensity ratio of the D to G peaks (I(D)/I(G)) was calculated to evaluate the defect density of the graphene [35, 36]. The I(D)/I(G) ratio increase with increased graphene's defects density. Since there are various defects present in graphene [37], the intensity ratios of the D and D′ peaks were analyzed to determine the prevailing defect type [38, 39]. Notably, the I(D)/I(D′) ratio 7 is typical for vacancies, the I(D)/I(D′) ratio 3.5 is typical for boundary defects, and the ratio 1.3 is typical for on-site defects. The positions of the G and 2D peaks (Pos(G) and Pos(2D)) were considered as parameters sensitive to graphene doping and stress [40, 41].

The surface morphology and current of the samples were investigated using atomic force microscopy (AFM, NanoWizard®3, JPK Instruments, Bruker Nano GmbH, Berlin, Germany). Morphological images were acquired with an ACTA probe (Applied NanoStructures, Inc., Mountain View, CA, USA) operating in the tapping mode with a tip radius of curvature of 6 nm. The surface current, which serves as a measure of the electrical conductivity of the samples, was examined using contact-mode conductive atomic force microscopy (C-AFM) with a Pt/Ir-coated ANSCM-PT silicon tip probe (thickness: 25 ± 5 nm; App-Nano, Mountain View, CA, USA). Both the reflex and tip sides of the probe were coated. The spring constant of the ANSCM probe was 1.6 N m^{-1} with a tetrahedral tip shape, a radius of curvature (ROC) of 30 nm, a height of 14–16 μm, and a frequency of 61 kHz. Ag electrodes were fabricated on the graphene layer to investigate the surface contact current. The surface current was measured as a function of the applied bias voltage (−10 to 10 mV). All the measurements were performed at room temperature in ambient air with a slight noise of 55 fA at a current gain of 1×.

The current-voltage (I–V) characteristics were measured using a Keithley 6487 picoampermeter/voltage source. The measurements were performed at several points on the sample to evaluate the possible dispersion of the characteristics. The photovoltaic and photoelectric properties of the fabricated devices were investigated in three different regimes. These were the dark mode (I–V characteristic measured in the dark), UV mode (when the sample was illuminated by a 406 nm wavelength light-emitting diode (LED)), and IR mode (when the sample was illuminated by an 800 nm wavelength light-emitting diode). The currents supplied to the LEDs were selected to ensure the same optical power (5.2 mW) between different measurement modes. Diode behavior was studied by examining the reverse current (0.5 V) measured in the dark. The photovoltaic parameters (short-circuit

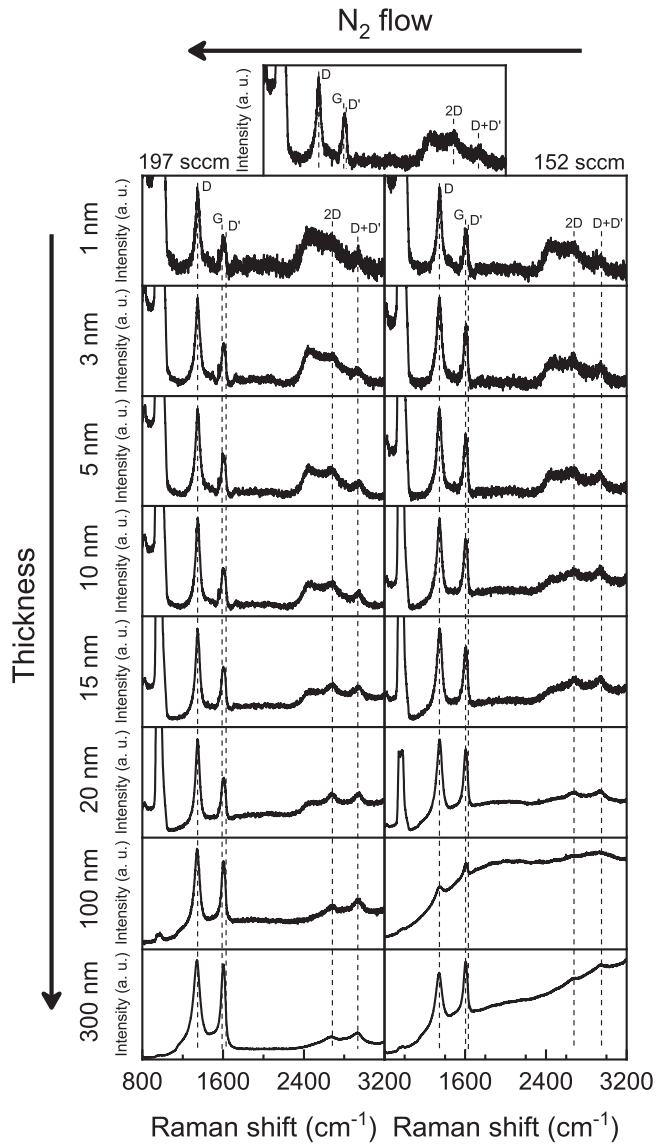

Figure 1. Typical Raman scattering spectra of the graphene synthesized on the h-BN interlayers of the different thickness. The reference spectra of the graphene synthesized directly on the Si(100) is on the top.

current (I_{SC}) and open-circuit voltage (U_{OC})) were estimated using the I-V characteristics measured under illumination. The photocurrent was calculated as the difference between the reverse current measured under illumination and that measured in the dark: In this case, the reverse measurement voltage was 0.5 V.

3. Results and discussion

The structures of the samples were investigated using Raman scattering spectroscopy. Typical spectra of h-BN interlayers are shown in figure S1. The Raman scattering spectra of graphene synthesized on different h-BN interlayers and the reference sample grown directly on Si(100) are presented in figure 1. G, 2D, D+D′, and D+D′ peaks were observed. A defect-related D peak was observed in all samples. The D peak was positioned at ~1347 cm^{-1} in the Raman spectrum of graphene synthesized on Si(100). The main h-BN Raman peak was observed at ~1370 cm^{-1} (see figure S1 [31]). It can be stated that an essential decrease in the graphene defect density and growth of the defect-free graphene was not achieved by using the HIPIMS-deposited h-BN interlayer. However, the h-BN interlayer provides other benefits, as explained later in this paper. It must be mentioned that for graphene directly synthesized on the h-BN interlayer grown by chemical vapor deposition on the SiO_2 film [30], the I(D)/I(G) ratio was similar to that in the present study. On the other hand, in present study, 2D peak was significantly more pronounced compared to the results reported in [30], where the 2D peak was almost invisible [30]. The defect-related D′ peak is presented as a G-peak shoulder. Luminescence background was observed in the Raman spectra of the samples deposited on thicker h-BN interlayers. This was

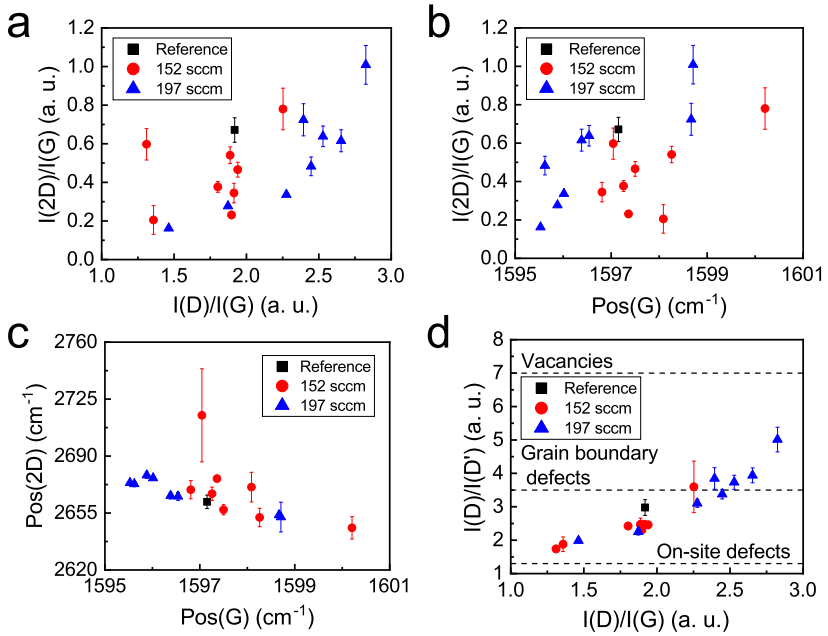

Figure 2. Interdependencies of Raman parameters. I(2D)/I(G) versus I(D)/I(G) (a); I(2D)/I(G) versus Pos(G) (b); Pos(2D) versus Pos (G) (c); I(D)/I(D′) versus I(D)/I(G) (d). Error bars show the dispersion of Raman parameters within the same sample.

more pronounced when h-BN interlayers were deposited using 152 sccm nitrogen gas flow. This is in good accordance with the peculiarities of the h-BN interlayer spectra—for h-BN films deposited using 152 sccm N_2 gas flow, significant luminescence background and luminescence lumps were observed (figure S2 and [31]) due to the formation of B–H and C–H bonds [31]. It should be mentioned that in the case of the graphene synthesized on the thicker h-BN interlayers, the 2D peak was less intensive than D+D′. This behavior is typical for hydrogenated graphene [42–45]. A similar luminescence background was observed previously in graphene directly synthesized on h-BN interlayers grown by CVD on SiO_2 substrates [30] and on catalytic copper foil [26], indicating common characteristics independent of substrate choice.

Subsequently, the Raman scattering spectra of the graphene samples were analyzed. As mentioned above, the I(2D)/I(G) ratio was proportional to the number of graphene layers [34]. Simultaneously, the presence of defects and doping can significantly reduce the I(2D)/I(G) ratio [35, 40, 46, 47]. In particular, the I(2D)/I(G) ratio decreases, and the G peak position shifts to higher wavenumbers (upshifted) because of doping [40, 47]. However, in our case, the I(2D)/I(G) ratio tended to increase with the I(D)/I(G) ratio and Pos(G) upshifting (figure 2). Thus, the I(2D)/I(G) ratio can be used to evaluate the number of graphene layers.

Pos(2D) was downshifted with Pos(G) upshift (figure 2). Some deviation from this tendency was only the Pos (2D) of the graphene synthesized on the 1 nm thickness h-BN interlayer deposited using a 152 sccm N_2 gas flow. The Pos(2D) downshift with Pos(G) is typical for n-type doped graphene [40, 41]. A similar behavior reported in our previous studies on graphene directly synthesized on Si(100) substrates was explained by the - substrate-induced self-doping of graphene [20, 32, 48]. It should be noted that graphene self-doping effects were also reported for graphene directly synthesized on the h-BN interlayer grown by chemical vapor deposition onto the SiO_2 film [30] and for h-BN and graphene layers grown by CVD on catalytic substrates and subsequently transferred onto SiO_2 [49].

A single deviation from these clear trends was observed for the graphene synthesized on the 100 nm thick h-BN interlayer deposited using a 152 sccm nitrogen flow, showing anomalously high Pos(2D) values (~2720 cm^{-1}) and significant dispersion. Such elevated Pos(2D) values may indicate accidental local p-type doping due to adsorbates or surface contamination, resulting in spatially varying doping characteristics and increased uncertainty within this particular sample [40, 41]. However, this isolated anomaly does not compromise the robustness or clarity of the overall trends across all other samples. Although repeating this isolated measurement was beyond the scope of the current work, future targeted studies could further clarify this minor deviation. Exact Raman parameter values of samples and their corresponding h-BN interlayer thicknesses can be seen in table S1.

It must be mentioned that exfoliated graphene placed on exfoliated h-BN exhibited reduced unintentional self-doping compared to graphene on SiO2 [50]. Now, one can see that graphene self-doping reduction can be achieved using the h-BN films deposited reactive magnetron sputtering, the technology compatible with large-

area industrial-scale deposition and direct graphene synthesis. Regarding the possible source of substrate-induced graphene self-doping, it should be mentioned that in the case of h-BN grown by CVD on catalytic Cu foil, the formation of surface defects (presence of amorphous BN or cubic BN clusters in the film) and presence of impurities (BxCyNz particles) have been reported, resulting in graphene self-doping [51]. In our case, a similar behavior was assumed. In addition, defects may be created because of the possible interactions between graphene and the h-BN interlayer during graphene synthesis [52]. The abovementioned defects and impurities can induce additional h-BN surface potentials and their local variations, resulting in self-doping of graphene.

The I(D)/I(D′) ratio increased with the I(D)/I(G) ratio. Thus, the I(D)/I(G) ratios of the samples with I(D)/I(D′) ratios close to those of graphene-containing on-site defects were the lowest. It should be mentioned that graphene on-site defects are usually associated with hydrogen bonding to graphene [39]. As pointed out above, the D + D′ peak was more intense than the 2D peak. This also supports the hypothesis of graphene hydrogenation [42–45]. No relationship between Pos(G) and I(D)/I(D′) was found, indicating that the - n-type graphene self-doping observed in this study was not related to graphene hydrogenation.

The effects of the h-BN interlayer on the structure and electronic properties of the synthesized graphene were investigated (figure 3). The defect density increased and the number of graphene layers decreased with the insertion of the boron nitride interlayer. An increase in the h-BN interlayer thickness resulted in a subsequent decrease in the I(D)/I(G) ratio and an increase in the number of graphene layers. With the insertion of the ultrathin h-BN interlayer, Pos(G) was upshifted and Pos(2D) was downshifted. Subsequently, Pos(G) downshifted and Pos(2D) upshifted with increasing boron nitride interlayer thickness.

One can see that Pos(G) and Pos(2D) shift towards the values typical for undoped and stress free graphene ($1581.6 \pm 0.2\ cm^{-1}$ and $2676.9 \pm 0.7\ cm^{-1}$, respectively [41]) with increased h BN film thickness when the h BN interlayer is thicker than 5 nm. This indicates reduced self-doping of graphene. However, self-doping has not yet been completely eliminated. The insertion of the h BN interlayer also affects the prevailing defect type in graphene, as can be seen in the I(D)/I(D′) versus h-BN interlayer thickness plot (figure 3(e)). In addition to the prevailing boundary defects typical of directly synthesized graphene, the 1 nm thick BN interlayer promoted the formation of vacancy defects. In the case of graphene grown on a 100 nm or thicker boron nitride interlayer, hydrogenation related to on-site defects and boundary defects dominated.

The structure of the grown graphene was investigated by AFM study of the surface morphology and conductivity of the samples to reveal the peculiarities of graphene growth on HIPIMS-deposited h-BN and graphene electronic properties. The Si/SiO_2 substrate was much smoother than the - h-BN film (figure 4). An aberrant grainy but smooth surface, with a root mean square roughness R_q of 0.64 nm, and grain sizes of 20 , 15 , and 3 nm in length, width, and height, respectively, was observed. After graphene deposition, the topography showed little to no change. However, the R_q value changed significantly to 1.68 nm. Similarly, the surface current signal increased to 3.77 pA (table S2). Both h-BN and graphene deposited on it showed a similar increase in R_q with increasing h-BN thickness. The graphene surface roughness clearly increased with the substrate surface roughness, and in all cases, the R_q of graphene was slightly larger than that h-BN interlayer R_q (figure S3). The h-BN thin film surface current readouts were similar to the background signal and did not exceed 1.5–2 pA. When the thickness of h-BN was increased to 110 nm, one can observe hexagonal structures with lengths, widths, and heights of 100 nm, 80 nm, and 15 nm were obtained. In this sample, there is an increase in R_q to 5.55 nm and the current value increase to 51.9 pA after graphene deposition, whereas the topography view seems indifferent. Further increasing the thickness of h-BN to 330 nm, a typical hexagonally shaped surface, with $R_q = 14.83$ nm and the size of the structural element 220 nm, 200 nm, and 40 nm in length, width, and height, can be observed. In this case, graphene deposition noticeably changed the surface morphology, increasing R_q to 18.86 nm. The grain sizes, in terms of length, width, and height, were 220, 60 , and 50 nm, respectively. For a given h-BN thickness of 330 nm, an increase in the average surface current signal (6.6 pA) was observed. The h-BN film composition was also important. The graphene synthesized on the 100 nm thickness h-BN film grown using different N_2 gas flows (152 sccm) was smoother, and its surface current was somewhat lower (32 pA compared to 52 pA). Hexagonally shaped structures were observed. From figure 5, it can be seen that, with an increase in R_q of graphene deposited on h-BN, the surface current signal increases and reaches a maximum value when $R_q = 5.55$ nm. The surface current signal decreases when a further increase in R_q is observed. The topographical parameters are listed in table S2. No relationship was observed between graphene surface conductivity and self-doping (figure S4). However, it should be noted that despite the h-BN films' surface roughness being much larger than the roughness of the SiO_2 film or Si(100) and despite the possible presence of B–H and C–H bonds in some h-BN films used in the present study (see [31] figure S1), reduced graphene self-doping was achieved, similar to the cases of exfoliated or transferred graphene and h-BN stacks[49, 50, 52].

In summary, we show that the synthesis of h-BN thin films on a Si/SiO_2 substrate using a N_2 gas flow of 197 sccm yields a hexagonal boron nitride surface with distinct 220 nm × 200 nm grains in length and width, respectively, with varying heights. Subsequently, the deposited graphene exhibits grain narrowing and

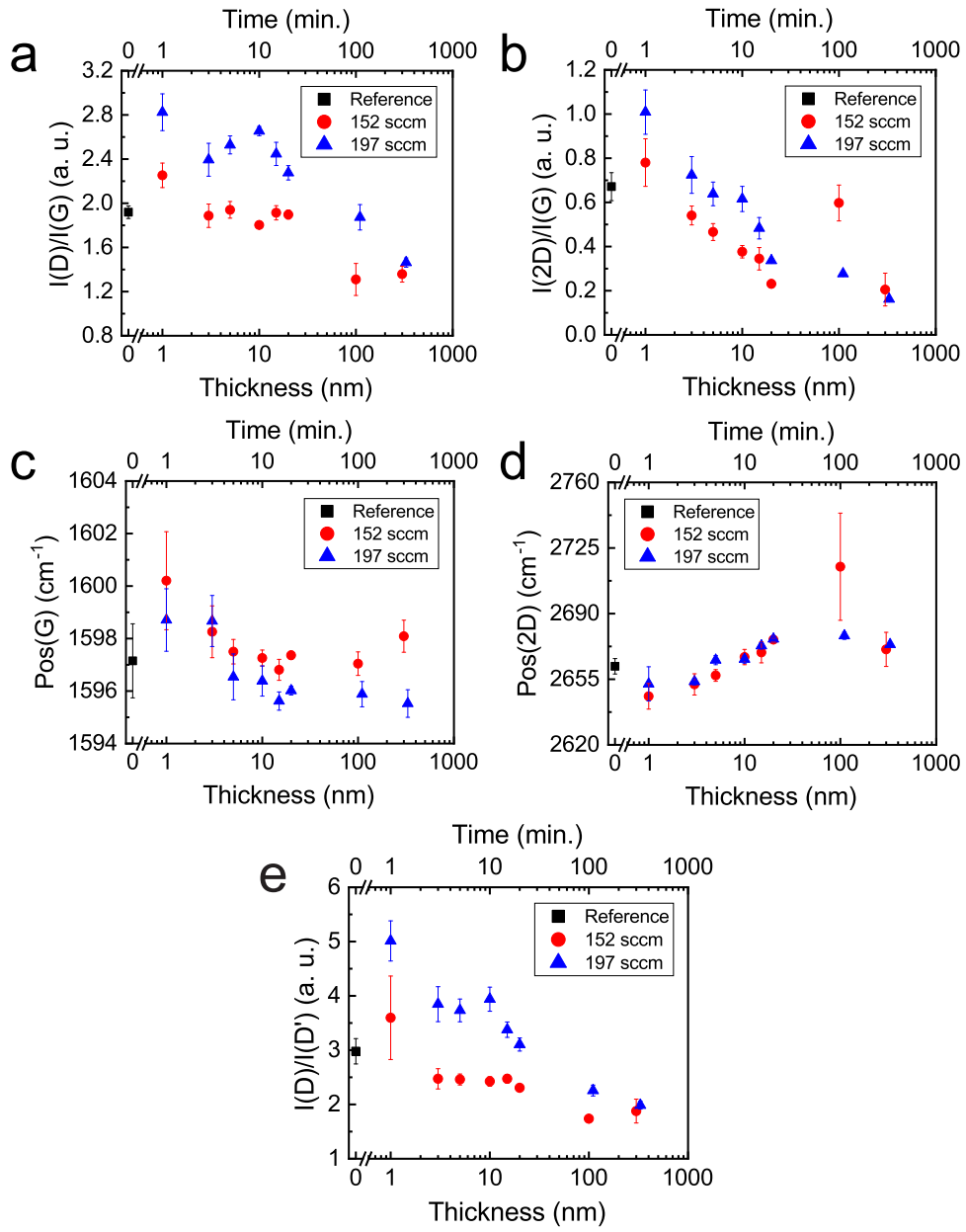

Figure 3. H-BN interlayer thickness effects on the I(D)/I(G) (a), I(2D)/I(G) (b), Pos(G) (c), Pos(2D) (d), I(D)/I(D′) (e). Error bars show the dispersion of Raman parameters within the same sample.

heightening. The average surface current signals increased because of the notable differences in the grain structure height. With high h-BN thickness, the surface current decreased. However, a relatively high surface current region was still observed in the sample.

Typical current-voltage (I–V) characteristics of the graphene/h-BN/Si(100) and graphene/Si(100) diodes are presented in figure 6 (I–V curves of individual samples are shown in figures S5–S17). In all the cases, the insertion of the h-BN interlayer resulted in an increased forward voltage. However, linear or quasi-linear reverse I-V characteristics, typical for directly synthesized graphene/Si(100) heterojunctions [32], were observed for nearly all samples. Thus, the primary reverse current charge transport mechanism is tunneling [32]. The insertion of the h-BN interlayer did not reduce the leakage current of the graphene/Si(100) heterojunction (figures 6, 7(a)). The leakage currents of the graphene/h-BN/Si(100) with an interlayer grown using 152 sccm nitrogen gas flow were higher than those of h-BN deposited using 197 sccm N_2 gas flow. This is likely related to the much higher carbon content in the films grown using a 152 sccm nitrogen gas flow (>15 at% versus ~3 at% [31]). However, it can be seen in figures 7(b), (c) that the h-BN interlayer can be used to increase the diode photocurrent and short circuit current. The effect was much more pronounced when the interlayer was grown under a 152 sccm N_2 gas flow. It can be seen that the photocurrent and short-circuit current non-monotonically depended on the thickness; the lowest photocurrent and the smallest short-circuit current were observed for

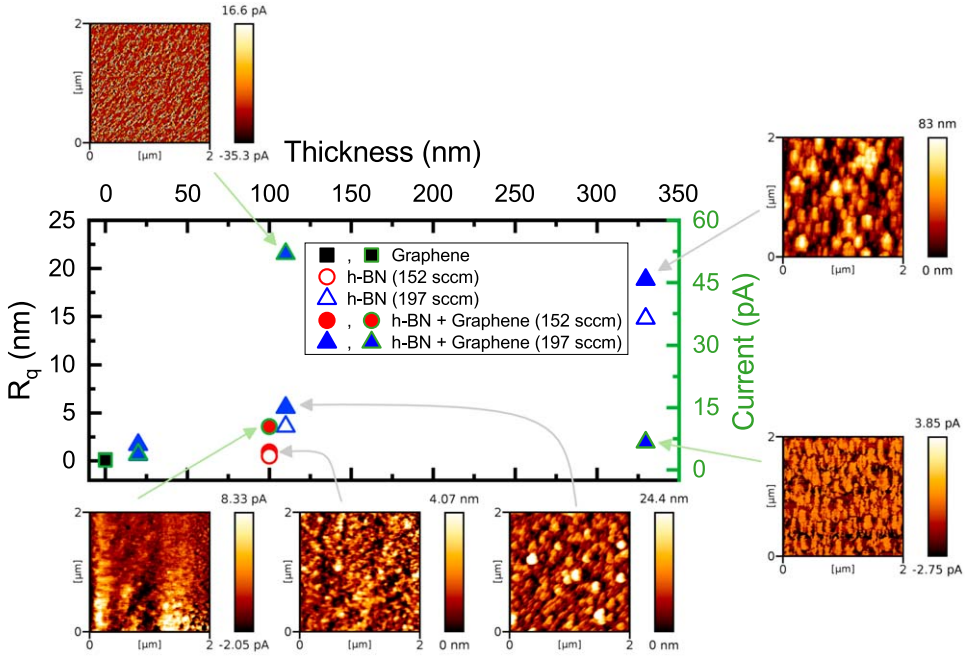

Figure 4. The dependence of the surface current (green axis and outline) and the root mean square roughness (R_q) (black axis) on the thickness of the h-BH thin film. Sample colors follow same style as in previous plots, where different N2 flows used during h-BN deposition are denoted with red circle (152 sccm) and blue triangle (197 sccm). Reference graphene sample is shown as black square. Sample points outlined with green color indicate a C-AFM value which can be deduced from green axis on the right side. AFM and C-AFM images show characteristic graphene/h-BN/Si(100) samples and corresponding points in the plot.

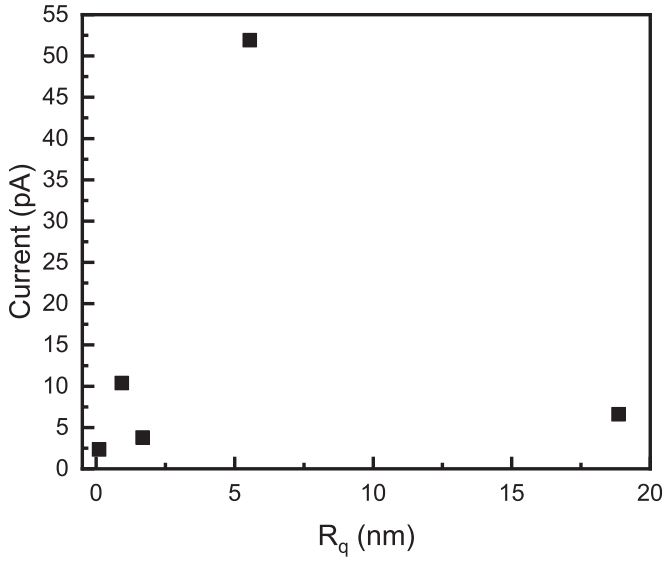

Figure 5. Graphene/h-BN/Si/SiO_2 surface current versus R_q.

samples fabricated using a 5–15 nm thick interlayer. The average open-circuit voltage of the graphene/h-BN/Si (100) diode was almost always higher than that of the graphene/Si diode. It should be mentioned that excitation by IR light for most samples resulted in a higher photocurrent, short-circuit current, and open-circuit voltage than UV light excitation. In our previous study, similar behavior was observed for the electrical and photovoltaic properties of graphene/Si(100) heterojunctions [32].

No clear dependence of the electrical and photoelectric properties of the samples on the Raman scattering spectral parameters was observed (figure S5). However, some weak expression tendencies were observed. The average reverse dark current decreased with an increase in the graphene defect density and number of layers. Thus, the graphene hydrogenation should be minimized to decrease the reverse dark current. The short-circuit current and photocurrent increased with Pos(G) upshift. The I_{SC} and photocurrent initially decreased and then

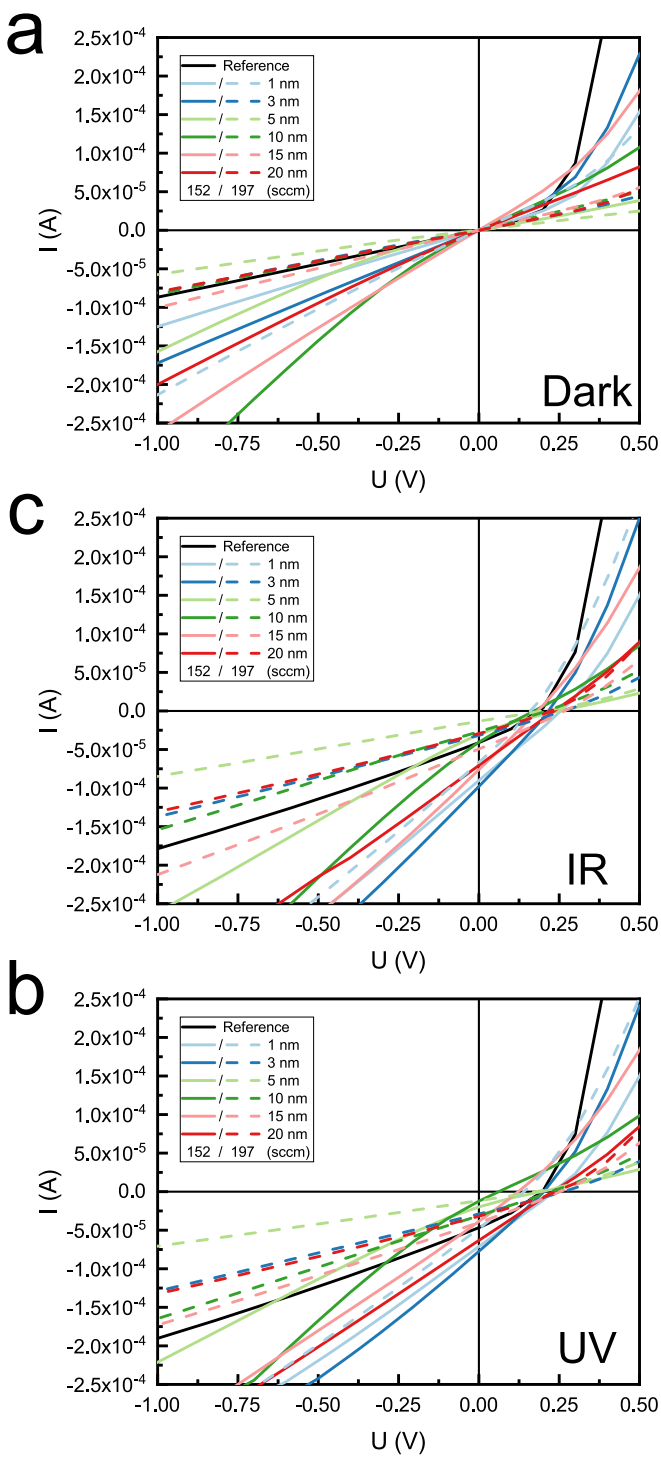

Figure 6. Graphene/h-BN/Si(100) I-V curves under no (a), IR (b) and UV (c) illumination.

increased with the Pos(2D) upshift. It can be assumed that graphene self-doping may be beneficial for increasing the photocurrent and the short-circuit current. The open-circuit voltage initially increased with defect density and subsequently decreased. However, no U_{OC} dependence on the I(D)/I(D′) ratio was observed, indicating that this behavior is not related to the prevailing defect type.

It should be mentioned that, in our previous study, the reverse current decreased with increasing graphene self-doping level for graphene/Si(100) diodes [32]. However, in the case of graphene/Si(100) heterojunctions, silicon surface pre-treatment significantly affected the electrical and photovoltaic properties of the fabricated diodes. Notably, in the case of the U_{OC}, surface pre-treatment is much more important than the graphene structure [32]. In that study, the I_{SC} tended to increase with reduced graphene self-doping. However, silicon surface pre-treatment conditions are also critical. It should be noted that there were more variables in this study. Notably, along with differences in the graphene's structure and electronic properties, there are factors of the

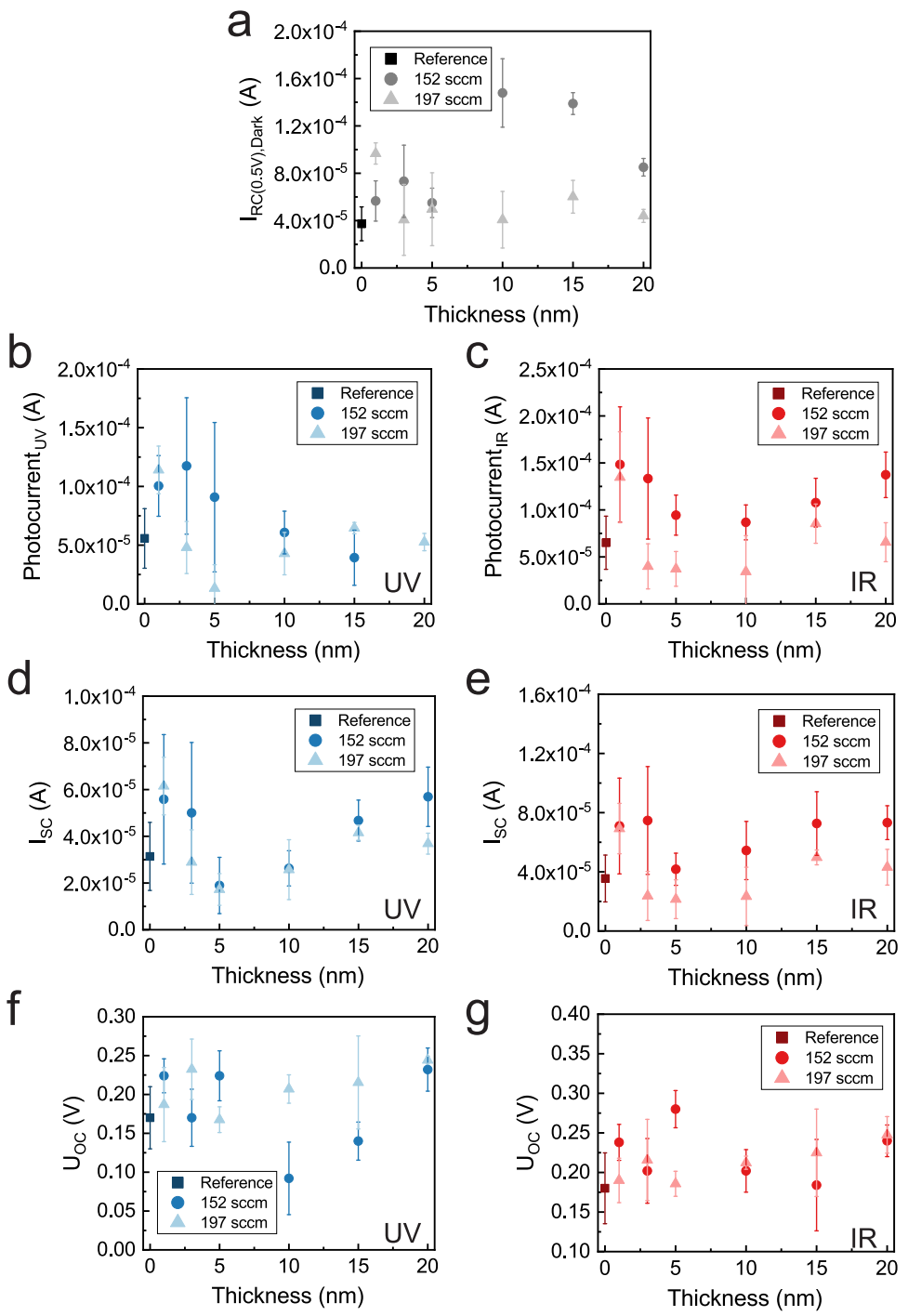

Figure 7. Graphene/h-BN/Si(100) diodes electrical and photoelectric properties dependence on the h-BN interlayer thickness: dark current (a), photocurrent (UV) (b), photocurrent (IR) (c), short circuit current (UV) (d), short circuit current (IR) (e), open circuit voltage (UV) (f), open circuit voltage (IR) (g). Error bars show the dispersion of the optoelectronic parameters within the same sample.

different h-BN film compositions or h-BN interlayer thicknesses, in addition to the variation in the film roughness. In addition, it can be assumed that in the case of the thinnest hexagonal boron nitride interlayer, the boron nitride film is - discontinuous. Competition between the abovementioned factors may hide the possible influence of the graphene structure, electronic properties, and h-BN interlayer on the electrical and photoelectric properties of graphene/h-BN/Si(100) diodes.

Notably, in the case of graphene/Si heterojunction solar cells fabricated using transferred graphene, the insertion of the h-BN interlayer significantly increased the open-circuit voltage and short-circuit current of the solar cell [10, 53–58]. In our case, a significant increase in the short-circuit current and open-circuit voltage was observed when magnetron sputter deposited h-BN films were used instead of transferred high-crystallinity h-BN flakes. In particular, the average short-circuit current and photocurrent nearly doubled, and the average

IR-light-excited open-circuit voltage increased by ~100 mV (figures 7 and S18). This improvement is comparable to the results reported for transferred graphene/Si solar cells enhanced by a transferred h-BN interlayer [10, 53, 58]. Thus, h-BN interlayers deposited by reactive high-power impulse magnetron sputtering can be effectively used to improve the photoelectric and photovoltaic properties of graphene/Si solar cells.

4. Conclusions

The effects of h-BN interlayer composition and thickness on the structure, morphology, and electrical properties of graphene and graphene-based devices were studied. Defect-free graphene was not grown using the HIPIMS-deposited h-BN interlayer. However, it was found that the graphene self-doping, attributed mainly to substrate-induced effects, could be partially controlled, and the graphene/Si(100) diode photocurrent, short-circuit current, and open-circuit voltage could be significantly increased by inserting an h-BN interlayer. The defect type of prevailing graphene can be changed by varying the boron interlayer thickness. The graphene layers grown on the boron nitride films were significantly rougher than those grown on the SiO_2 films. The surface current of graphene grown on h-BN was much higher than that of graphene synthesized on the SiO_2 film. No relationship was found between graphene surface conductivity and graphene self-doping. However, it must be mentioned that despite the h-BN film surface roughness being much larger than the roughness of the SiO_2 film or Si(100) and the possible presence of B–H and C–H bonds in some h-BN films, reduced graphene self-doping was achieved. Tunneling is the primary reverse current charge transfer mechanism, similar to graphene/Si(100) diodes, and h-BN interlayers cannot decrease the reverse dark current. Despite all the abovementioned circumstances, the insertion of the h-BN interlayer resulted in a photocurrent and a significant increase in the photocurrent, short circuit current, and open circuit voltage compared to the graphene/Si(100) heterojunction. Notably, the average short-circuit current and photocurrent nearly doubled, and the average IR-light-excited open-circuit voltage increased by ~100 mV. Thus, h-BN interlayers deposited by reactive high-power impulse magnetron sputtering can be effectively used to improve the photoelectric and photovoltaic properties of graphene/Si solar cells. The observed effects of the h-BN interlayer on the properties of the graphene/Si(100) diodes were explained by the competition between the influence of the graphene structure and electronic properties and the one hand and impact of different h-BN film compositions, thicknesses, and roughness.

Acknowledgments

This study was supported by the Research Council of Lithuania (Proposal No. P-MIP-22-235; Contract No S-MIP-22-67).

Conflicts of interest

The authors declare no conflict of interest.

Data availability statement

All data that support the findings of this study are included within the article (and any supplementary files).

Funding

This study was funded by the Research Council of Lithuania (Proposal No. P-MIP-22-235; Contract No S-MIP-22-67).

ORCID iDs

Šarūnas Meškinis https://orcid.org/0000-0001-9622-7573
Šarūnas Jankauskas https://orcid.org/0000-0001-6347-5167
Asta Guobienė https://orcid.org/0000-0002-1421-0012

References

[1] Lee C, Wei X, Kysar J W and Hone J 2008 Measurement of the elastic properties and intrinsic strength of monolayer graphene *Science (1979)* **321** 385–8
[2] Nair R R, Blake P, Grigorenko A N, Novoselov K S, Booth T J, Stauber T, Peres N M R and Geim A K 2008 Fine structure constant defines visual transparency of graphene *Science (1979)* **320** 1308
[3] Morozov S V, Novoselov K S, Katsnelson M I, Schedin F, Elias D C, Jaszczak J A and Geim A K 2008 Giant intrinsic carrier mobilities in graphene and its bilayer *Phys. Rev. Lett.* **100** 016602
[4] Lee J-Y, Connor S T, Cui Y and Peumans P 2008 Solution-processed metal nanowire mesh transparent electrodes *Nano Lett.* **8** 689–92
[5] Zhang Z, Du J, Zhang D, Sun H, Yin L, Ma L, Chen J, Ma D, Cheng H-M and Ren W 2017 Rosin-enabled ultraclean and damage-free transfer of graphene for large-area flexible organic light-emitting diodes *Nat. Commun.* **8** 14560
[6] Wu M, Wang Z, Wang X and Yu J 2018 High-performance organic light-emitting photodetector fabricated by separating photodetective center from emissive layer without luminance trade-off *Opt. Lett.* **43** 4502
[7] Lin X *et al* 2022 *In situ* growth of graphene on both sides of a Cu–Ni alloy electrode for perovskite solar cells with improved stability *Nat. Energy* **7** 520–7
[8] Mahalingam S, Manap A, Omar A, Low F W, Afandi N F, Chia C H and Rahim N A 2021 Functionalized graphene quantum dots for dye-sensitized solar cell: key challenges, recent developments and future prospects *Renew. Sustain. Energy Rev.* **144** 110999
[9] Nasir S, Johrin N, Low W, Moh P Y, Megat Hasnan M M I, bin, Ghosh B K and Chee F P 2024 Review—development of graphene-based photodiode device: synthesis, deposition, and characterization *ECS J. Solid State Sci. Technol.* **13** 121001
[10] Fallahazad P 2023 Rational and key strategies toward enhancing the performance of graphene/silicon solar cells *Mater Adv.* **4** 1876–99
[11] Sun M, Wang S, Liang Y, Wang C, Zhang Y, Liu H, Zhang Y and Han L 2025 Flexible graphene field-effect transistors and their application in flexible biomedical sensing *Nanomicro Lett.* **17** 34
[12] Yan K *et al* 2015 High-performance graphene-based hole conductor-free perovskite solar cells: schottky junction enhanced hole extraction and electron blocking *Small* **11** 2269–74
[13] Yi K, Liu D, Chen X, Yang J, Wei D, Liu Y and Wei D 2021 Plasma-enhanced chemical vapor deposition of two-dimensional materials for applications *Acc. Chem. Res.* **54** 1011–22
[14] Fang Y, Zhou K, Wei W, Zhang J and Sun J 2024 Recent advances in batch production of transfer-free graphene *Nanoscale* **16** 10522–32
[15] Chen Z *et al* 2021 Direct growth of wafer-scale highly oriented graphene on sapphire *Sci. Adv.* **7** 1–7
[16] Mishra N *et al* 2019 Wafer-scale synthesis of graphene on sapphire: toward fab-compatible graphene *Small* **15** 1904906
[17] Wang Y, Zhang M, Li P, Chen X, Xue Z, Wu X and Di Z 2022 Structural properties of grain boundary in graphene grown on germanium substrates with different orientations *Appl. Phys. Lett.* **121** 011901
[18] Wang H, Xue X, Jiang Q, Wang Y, Geng D, Cai L, Wang L, Xu Z and Yu G 2019 Primary nucleation-dominated chemical vapor deposition growth for uniform graphene monolayers on dielectric substrate *J. Am. Chem. Soc.* **141** 11004–8
[19] Shi Q *et al* 2020 Substrate developments for the chemical vapor deposition synthesis of graphene *Adv. Mater. Interfaces* **7** 1902024
[20] Meškinis Š, Vasiliauskas A, Guobienė A, Talaikis M, Niaura G and Gudaitis R 2022 The direct growth of planar and vertical graphene on Si(100) *via* microwave plasma chemical vapor deposition: synthesis conditions effects *RSC Adv.* **12** 18759–72
[21] Meškinis Š *et al* 2023 Biosensor based on graphene directly grown by MW-PECVD for detection of COVID-19 Spike (S) protein and its entry receptor ACE2 *Nanomaterials* **13** 2373
[22] Chugh S, Mehta R, Lu N, Dios F D, Kim M J and Chen Z 2015 Comparison of graphene growth on arbitrary non-catalytic substrates using low-temperature PECVD *Carbon N Y* **93** 393–9
[23] Khan A, Islam S M, Ahmed S, Kumar R R, Habib M R, Huang K, Hu M, Yu X and Yang D 2018 Direct CVD growth of graphene on technologically important dielectric and semiconducting substrates *Adv. Sci.* **5** 1800050
[24] Han Z, Li M, Li L, Jiao F, Wei Z, Geng D and Hu W 2021 When graphene meets white graphene—recent advances in the construction of graphene and *h*-BN heterostructures *Nanoscale* **13** 13174–94
[25] Yang W *et al* 2013 Epitaxial growth of single-domain graphene on hexagonal boron nitride *Nat. Mater.* **12** 792–7
[26] Wang M *et al* 2013 A platform for large-scale graphene electronics—CVD growth of single-layer graphene on CVD-grown hexagonal boron nitride *Adv. Mater.* **25** 2746–52
[27] Song X, Sun J, Qi Y, Gao T, Zhang Y and Liu Z 2016 Graphene/h-BN heterostructures: recent advances in controllable preparation and functional applications *Adv. Energy Mater.* **6** 1600541
[28] Huang M, Deng B, Dong F, Zhang L, Zhang Z and Chen P 2021 Substrate engineering for CVD growth of single crystal graphene *Small Methods* **5** 2001213
[29] Gao W, Zhi G, Zhou M and Niu T 2024 Growth of single crystalline 2D materials beyond graphene on non-metallic substrates *Small* **20** 2311317
[30] Entani S, Takizawa M, Li S, Naramoto H and Sakai S 2019 Growth of graphene on SiO2 with hexagonal boron nitride buffer layer *Appl. Surf. Sci.* **475** 6–11
[31] Stankus V, Vasiliauskas A, Guobienė A, Andrulevičius M and Meškinis Š 2024 Synthesis and characterization of boron nitride thin films deposited by high-power impulse reactive magnetron sputtering *Molecules* **29** 5247
[32] Jankauskas Š, Gudaitis R, Vasiliauskas A, Guobienė A and Meškinis Š 2022 The graphene structure's effects on the current-voltage and photovoltaic characteristics of directly synthesized graphene/n-Si(100) Diodes *Nanomaterials* **12** 1640
[33] Glemža J, Palenskis V, Gudaitis R, Jankauskas Š, Guobienė A, Vasiliauskas A, Meškinis Š, Pralgauskaitė S and Matukas J 2022 Low-frequency noise of directly synthesized graphene/Si(100) junction *Diam. Relat. Mater.* **127** 109207
[34] Hwang J-S *et al* 2013 Imaging layer number and stacking order through formulating Raman fingerprints obtained from hexagonal single crystals of few layer graphene *Nanotechnology* **24** 015702
[35] Childres I, Jauregui L A, Tian J and Chen Y P 2011 Effect of oxygen plasma etching on graphene studied using Raman spectroscopy and electronic transport measurements *New J. Phys.* **13** 025008
[36] Dresselhaus M S, Jorio A, Souza Filho A G and Saito R 2010 Defect characterization in graphene and carbon nanotubes using Raman spectroscopy *Philosophical Transactions of the Royal Society A: Mathematical, Physical and Engineering Sciences* **368** 5355–77
[37] Bhatt M, Kim H and Kim G 2022 Various defects in graphene: a review *RSC Adv.* **12** 21520–47
[38] Eckmann A, Felten A, Mishchenko A, Britnell L, Krupke R, Novoselov K S and Casiraghi C 2012 Probing the Nature of Defects in Graphene by Raman Spectroscopy *Nano Lett.* **12** 3925–30
[39] Venezuela P, Lazzeri M and Mauri F 2011 Theory of double-resonant Raman spectra in graphene: intensity and line shape of defect-induced and two-phonon bands *Phys. Rev. B* **84** 035433
[40] Casiraghi C 2009 Probing disorder and charged impurities in graphene by Raman spectroscopy *Rapid Research Letters* **3** 175–7

[41] Lee J E, Ahn G, Shim J, Lee Y S and Ryu S 2012 Optical separation of mechanical strain from charge doping in graphene *Nat. Commun.* **3** 1024
[42] Luo Z, Yu T, Kim K, Ni Z, You Y, Lim S, Shen Z, Wang S and Lin J 2009 Thickness-dependent reversible hydrogenation of graphene layers *ACS Nano* **3** 1781–8
[43] Elias D C *et al* 2009 Control of graphene's properties by reversible hydrogenation: evidence for graphane *Science (1979)* **323** 610–3
[44] Melios C, Spencer S, Shard A, Strupiński W, Silva S R P and Kazakova O 2016 Surface and interface structure of quasi-free standing graphene on SiC *2D Mater.* **3** 025023
[45] Shtepliuk I, Ivanov I G, Iakimov T, Yakimova R, Kakanakova-Georgieva A, Fiorenza P and Giannazzo F 2019 Raman probing of hydrogen-intercalated graphene on Si-face 4H-SiC *Mater. Sci. Semicond. Process.* **96** 145–52
[46] Clapa M and Gaj J 2021 Behavior of graphene under glow discharge plasma *Sens Actuators A Phys.* **332** 113069
[47] Casiraghi C, Pisana S, Novoselov K S, Geim A K and Ferrari A C 2007 Raman fingerprint of charged impurities in graphene *Appl. Phys. Lett.* **91** 233108
[48] Gudaitis R, Lazauskas A, Jankauskas Š and Meškinis Š 2020 Catalyst-less and transfer-less synthesis of graphene on Si(100) using direct microwave plasma enhanced chemical vapor deposition and protective enclosures *Materials* **13** 5630
[49] Fukamachi S, Solís-Fernández P, Kawahara K, Tanaka D, Otake T, Lin Y-C, Suenaga K and Ago H 2023 Large-area synthesis and transfer of multilayer hexagonal boron nitride for enhanced graphene device arrays *Nat. Electron.* **6** 126–36
[50] Dean C R *et al* 2010 Boron nitride substrates for high-quality graphene electronics *Nat. Nanotechnol.* **5** 722–6
[51] Kim S, Kim B, Park S, Chang W S, Kang H, Kim S, Lee H and Kim S 2023 Hysteretic behavior of all CVD h-BN/graphene/h-BN heterostructure field-effect transistors by interfacial charge trap *Surfaces and Interfaces* **36** 102615
[52] Xu H, Wu J, Chen Y, Zhang H and Zhang J 2013 Substrate engineering by hexagonal boron nitride/SiO_2 for Hysteresis-free graphene FETs and large-scale graphene p–n junctions *Chem. Asian J.* **8** 2446–52
[53] Behura S K, Wang C, Wen Y and Berry V 2019 Graphene–semiconductor heterojunction sheds light on emerging photovoltaics *Nat. Photonics* **13** 312–8
[54] Huang K, Yu X, Cong J and Yang D 2018 Progress of graphene–silicon heterojunction photovoltaic devices *Adv. Mater. Interfaces* **5** 1801520
[55] Bhopal M F, Lee D W, Rehman A ur and Lee S H 2017 Past and future of graphene/silicon heterojunction solar cells: a review *J. Mater. Chem. C* **5** 10701–14
[56] Kong X, Zhang L, Liu B, Gao H, Zhang Y, Yan H and Song X 2019 Graphene/Si schottky solar cells: a review of recent advances and prospects *RSC Adv.* **9** 863–77
[57] Song L, Yu X and Yang D 2019 A review on graphene-silicon schottky junction interface *J. Alloys Compd.* **806** 63–70
[58] Meng J-H, Liu X, Zhang X-W, Zhang Y, Wang H-L, Yin Z-G, Zhang Y-Z, Liu H, You J-B and Yan H 2016 Interface engineering for highly efficient graphene-on-silicon schottky junction solar cells by introducing a hexagonal boron nitride interlayer *Nano Energy* **28** 44–50